

An Improved Hybrid Field Model for Calculating On-Load Performance of Interior Permanent-Magnet Motors

Zhaokai Li , Xiaoyan Huang , Member, IEEE, Lijian Wu , Senior Member, IEEE, He Zhang , Senior Member, IEEE, Tingna Shi , Member, IEEE, Yan Yan , Bowen Shi , and Geng Yang , Member, IEEE

Abstract—In this article, we developed an improved hybrid field model (IHFM) to predict the on-load performance of the interior permanent-magnet (IPM) motors considering both iron saturation and slotting effect. It combines the airgap analytical model based on the modified conformal mapping with the reluctance mesh method for stator and rotor. The reluctance mesh method can accurately predict the rotor saturation and tooth-tip saturation even their field distribution is complicated due to the armature reaction. Besides, IHFM will significantly accelerate computation speed using the analytical model for airgap region while keeping high accuracy. The finite-element analysis and experimental results of the flat-type and V-type IPM motors are demonstrated to verify the effectiveness of the proposed model.

Index Terms—Analytical model, conformal mapping, interior permanent-magnet (IPM) motor, reluctance mesh method, reluctance network.

I. INTRODUCTION

THE interior permanent-magnet (IPM) motor has the advantage of high torque, high power density, and high efficiency. It has been widely used and investigated in the research and industrial application. For the accurate prediction of IPM motors, finite-element (FE) analysis is one of the good choices because it can account for the nonlinearity of magnetic materials and, therefore, achieve high accuracy [1]. However, it consumes huge computation and lacks the insight for the motor design.

Manuscript received June 14, 2020; revised August 26, 2020 and September 23, 2020; accepted September 25, 2020. Date of publication October 13, 2020; date of current version June 28, 2021. This work was supported in part by the National Natural Science Foundation of China under Grant 51922095, in part by the Ningbo Science and Technology Innovation 2025 Major Project under Grant 2018B10001, and in part by the Key R&D Program of Zhejiang under Grant 2019C01075. (Corresponding author: Xiaoyan Huang.)

Zhaokai Li, Lijian Wu, Tingna Shi, Yan Yan, and Geng Yang are with the Zhejiang University, Hangzhou 310058, China (e-mail: lzk_zju@zju.edu.cn; ljw@zju.edu.cn; tnsi@zju.edu.cn; yan_yan@zju.edu.cn; yanggeng@zju.edu.cn).

Xiaoyan Huang is with the Zhejiang University Advanced Electrical Equipment Innovation Center, Hangzhou 310058, China (e-mail: xiaoyanhuang@zju.edu.cn).

He Zhang and Bowen Shi are with the University of Nottingham Ningbo China, Ningbo 315100, China (e-mail: he.zhang@nottingham.edu.cn; bowen.shi1@nottingham.edu.cn).

Color versions of one or more of the figures in this article are available online at <https://ieeexplore.ieee.org>.

Digital Object Identifier 10.1109/TIE.2020.3029477

In the stage of initial design and optimization, the circuit-based model and the analytical model are usually employed to save the calculation time. For the circuit-based model of IPM motors, a magnetic equivalent circuit model (MECM) calculates its lumped parameter based on the division of regular flux path [2]–[5], while a reluctance network method (RNM) defines the network reluctance (RN) according to the certain mesh rules [6], [7]. Hence, MECM can save much computation when calculating the magnetic field with the regular flux path and RNM exhibits high accuracy regardless of the complexity of field distribution. However, MECM has poor performance in calculating the flux density along the irregular flux path (e.g., airgap region and tooth-tip region), while RNM bears a huge computational burden compared with MECM [8]. Besides, both circuit-based models have the disadvantage of reconstruction of the circuit at different rotor positions, which significantly increases the complexity to calculate the time-varying performance.

As for the analytical model, the winding function theory is widely used to calculate the magnetic motive force (MMF) according to the winding distribution and obtain the airgap inverse function [9]–[11]. The rotor MMF function is modified in [12] to account for the pole-cap effect. However, these methods neglect the magnetic saturation and show low accuracy.

The modified winding function combined with MECM is proposed in [13]–[16]. The flux line in the IPM motor at different rotor position is investigated to obtain the new equivalent airgap function and computed the inductance under the on-load condition [13]. Besides, the harmonic component of the airgap flux density considering the pulsewidth modulation effect can be analyzed for magnet eddy-current loss calculation based on the combination of winding function and magnetic equivalent circuit (MEC) [14]. Elloumi *et al.* [16] analyzed the flux weakening capability of IPM motors using the modified winding function with simple MEC in the dq -axis and obtained good prediction accuracy. Compared with the original winding function model, these models have improved the calculation accuracy because they account for the magnetic potential drop in the iron region. However, the magnetic bridge saturation and tooth-tip saturation is too complex to be accurately modeled by simple MEC. Hence, an accurate stator and rotor permeance identification based on the finite-element analysis was combined

with the winding function theory to show the accurate iron saturation [17].

Compared with the winding function model, which is a one-dimensional (1-D) analytical model, the 2-D analytical model based on the Poisson or Laplace equation achieves higher accuracy for predicting the airgap field. It is extensively used in the surface-mounted permanent magnet (SPM) motors due to the accurate modeling of permanent magnet (PM) in the airgap region. The conformal mapping model based on one-pole-pitch region is proposed in [18] to predict the magnetic field of SPM motors. The one-pole-pitch region is necessary for the SPM motors because the PM equivalent current is placed inside the airgap region. Nevertheless, it can be optimized to one-slot conformal mapping for IPM motors as the PM equivalent current is on the interface between rotor and airgap. Hence, the calculation burden is decreased. For IPM motors, the complex permeance model combined with the finite-element method (FEM)-based slotless airgap field is proposed in [1]. However, it neglects the deformation of the circular path for predicting the airgap field and, therefore, introduces larger error with a smaller slot opening. The MECM combined with the analytical model based on the complex permeance function [19], [20] or subdomain technique [21]–[24] has been investigated to consider the stator saturation. Nevertheless, the rotor saturation is neglected in these models for SPM motors.

Unlike the SPM motor whose PM produced field can be analytically calculated in [19]–[24], the IPM motor cannot be directly analyzed using the 2-D analytical model since the rotor field distribution is complex and significantly affected by the armature reaction. Mirazimi and Kiyomarsi [25] proposed a conformal mapping model to represent the rotor saliency and stator slotting in the IPM motors. The airgap field was calculated using the conformal mapping technique but the bridge saturation is neglected. With the aid of MECM, the rotor and stator saturation were included in the improved analytical model based on the conformal mapping [26], [27]. The subdomain-based analytical model for IPM motors is combined with MECM to accurately predict the electromagnetic performance in [28] and [29]. By applying the boundary condition between the iron region and airgap region, the iron permeability can be iteratively calculated for spoke-type IPM motors [28] and multilayer IPM motors [29]. However, these 2-D analytical models in [26]–[29] can only analyze the open-circuit field of IPM motors. There are few papers about the 2-D analytical model for IPM motors under the on-load condition due to the complex rotor saturation.

In this article, a computationally efficient improved hybrid field model (IHFM) combining RNM with MECM is proposed to account for both slotting effect and saturation effect with high accuracy for IPM motors. The analytical airgap field calculation based on the one-slot conformal mapping is introduced to replace the large airgap RN. Hence, the RN and MEC will stay unchanged at any rotor position, which simplifies the network modeling. In the IPM motors, the armature reaction field has a significant influence on the rotor bridge saturation and tooth-tip saturation. Hence, a novel RNM is used to accurately capture the magnetic potential drop along the rotor and tooth surface, while MECM is introduced for the modeling of rotor yoke, stator yoke,

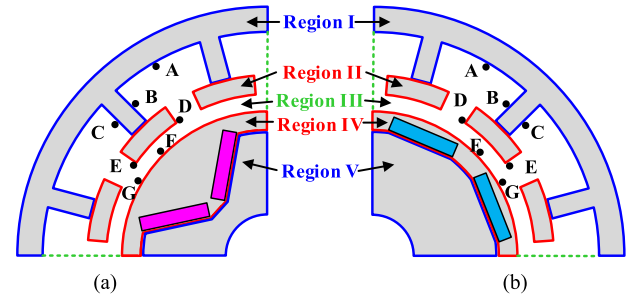


Fig. 1. Schematic view of IPM motors using IHFM. (a) V-type rotor. (b) Flat-type rotor.

and tooth body. IHFM makes the best of computation resource to analyze the IPM motors under the on-load condition with high accuracy and low computation. The finite-element analysis and experiments of two IPM motors with the flat-type rotor and V-type rotor have been carried out to validate the proposed model.

II. IMPROVED HYBRID FIELD MODEL

There are two ways to look into the IHFM. In the view of a 2-D analytical model, it incorporates the RNM and MECM to account for both PM-produced field and iron saturation. As a modified circuit-based model, the large airgap RN is replaced by flux sources using the analytical airgap solution, saving much calculation time and decreasing the complexity of network modeling. Fig. 1 shows the schematic view of IHFM for analyzing IPM motors. The region division with different calculation method is given as follows.

- 1) Region III (air-region) is represented by the analytical solution based on the one-slot conformal mapping.
- 2) Region II (tooth edge) and Region IV (rotor surface) are modeled using RN.
- 3) Region I (stator tooth and stator yoke) and Region V (rotor yoke) are calculated using MECM.

The coupling between the analytical model and RNM is based on the equivalent transformation between the equivalent virtual surface current and magnetic potential drop on the interface of Region III.

A. Novel Reluctance Network

For IPM motors, the flux path in the rotor bridge and stator tooth-tip is irregular under the on-load condition and it will significantly influence the airgap field distribution. Hence a novel mesh cell is proposed to model these important regions with complex flux path, as shown in Fig. 2. Only three reluctances are used in the modular mesh cell with a flux source representing the airgap field. The airgap flux source is the key to incorporating the analytical model into the RNM. The rotation of the rotor only changes the value of the airgap flux source and keeps the reluctance network unchanged. The airgap flux is obtained from the vector potential distribution as

$$\phi_{ak} = l_{ef}(A_{z1} - A_{z2}) \quad (1)$$

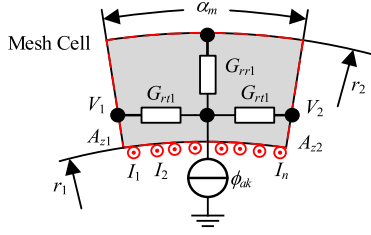


Fig. 2. Modular mesh cell for the reluctance network.

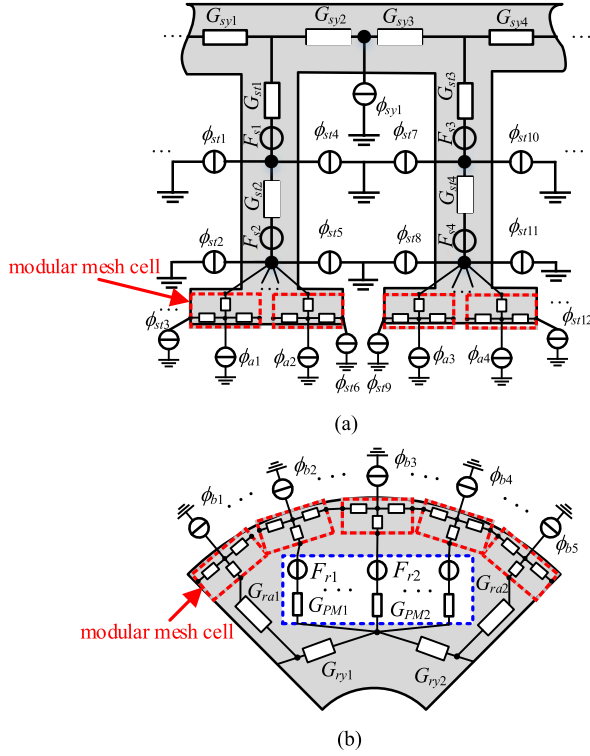


Fig. 3. RN and MEC for IPM motors. (a) Stator region. (b) Rotor region.

where l_{ef} is the effective length of the IPM motor. The radial and tangential iron reluctance in the novel mesh cell is calculated by

$$\begin{aligned} G_{rr1} &= \frac{\mu_r \alpha_m l_{ef}}{\ln(r_2/r_1)} \\ G_{rt1} &= \frac{2\mu_r l_{ef} \ln(r_2/r_1)}{\alpha_m} \end{aligned} \quad (2)$$

where α_m is the angle of sectorial reluctance. r_1 and r_2 are the internal and external radius.

Based on the rectangular mesh method and novel mesh cell, the corresponding RN can be automatically generated without *a priori* knowledge of flux path. Hence, the proposed RNM representing the stator tooth edge and rotor surface (see red box in Fig. 3) can be determined according to (2). As the airgap reluctances are replaced by the flux source, the calculation time will be shortened. Besides, the proposed RN is applicable for every rotor position, which is different from the dynamic RNM [8] or MECM [3]. In the IHFM, the number of modular mesh cells

in the pole-shoe region and along the rotor surface is selected according to the saturation level. For the rotor bridge region with high saturation, the criteria for the number of modular mesh cell is given as $G_{rt1} \gg G_{rr1}$ when using the same iron permeance. As for the pole-shoe region, the criterion of $G_{rt1} < G_{rr1}$ is obtained based on the lower iron saturation. Such a choice will reach a good compromise between the calculation efficiency and accuracy.

As for Regions I and V, their geometry is regular and the flux travels through these regions uniformly. Hence the MECM is proposed to calculate their magnetic potential distribution. In Fig. 3(a), the stator yoke reluctance G_{syk} and stator tooth reluctance G_{stk} can be expressed as [3]

$$\begin{aligned} G_{syk} &= \frac{\mu_r l_{ef} Q_s \ln(R_3/(R_3 - h_{sy}))}{\pi}, \quad k = 1, 2, \dots \\ G_{stk} &= \frac{\mu_r l_{ef} b_t}{2h_t}, \quad k = 1, 2, \dots \end{aligned} \quad (3)$$

where R_3 is the stator external radius and h_{sy} is the stator yoke height. Q_s is the slot number. b_t and h_t are the width and height of the stator tooth. In Fig. 3(b), the PM reluctance G_{PMk} is calculated as [3]

$$G_{PMk} = \frac{\mu_r l_{ef} b_{PM}}{2h_{PM}}, \quad k = 1, 2, \dots \quad (4)$$

where b_{PM} and h_{PM} are the width and height of PM. The rotor yoke iron G_{ryk} and the iron between PM G_{rak} is considered as trapezoidal and, therefore, they are expressed as

$$\begin{aligned} G_{rak} &= \frac{\mu_r l_{ef} (a_{trap} - b_{trap})}{h_{trap} \ln(a_{trap}/b_{trap})}, \quad k = 1, 2, \dots \\ G_{ryk} &= \frac{\mu_r l_{ef} h_{trap} \ln(a_{trap}/b_{trap})}{(a_{trap} - b_{trap})}, \quad k = 1, 2, \dots \end{aligned} \quad (5)$$

where a_{trap} , b_{trap} , and h_{trap} are the bases and height of the trapezoidal iron. The calculation of magnetic voltage source in the stator and rotor can be seen in [8].

For the slot region with air permeability, its analytical solution can be directly obtained. Therefore, the slot flux source flowing into the stator teeth and stator yoke is proposed to improve the accuracy rather than MECM, as shown in Fig. 3(a). It is calculated by

$$\begin{aligned} \phi_{st} &= l_{ef} (A_{zstk} - A_{zst(k+1)}) \\ \phi_{sy} &= l_{ef} (A_{zsyk} - A_{zsy(k+1)}) \end{aligned} \quad (6)$$

where A_{zsyk} and A_{zstk} are the vector potential on the slot bottom and on the left/right side of the slot region.

B. Analytical Model for Airgap Region

The keypoint of the IHFM is the accurate prediction of the airgap field. The analytical model based on the one-slot conformal mapping is proposed to calculate the airgap field distribution instead of RNM while achieving high accuracy. The calculation speed will be significantly improved as the magnetic potential node is decreased. Besides, the dynamic construction of RN is avoided to reduce the modeling complexity. To obtain the

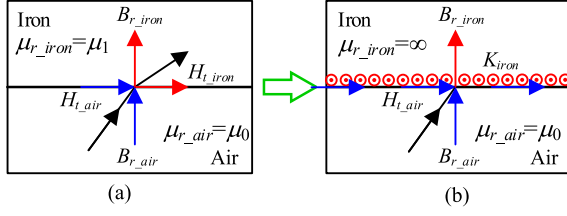


Fig. 4. (a) Original and (b) modified boundary condition for IHFM.

analytical airgap field solution of the IPM motor, the general boundary condition between airgap region and iron region with different permeability is listed as

$$\begin{cases} B_{r_air} = B_{r_iron} \\ H_{t_air} - H_{t_iron} = K_{iron} \end{cases} \quad (7)$$

Under the normal circumstances, there is no surface current sheet and, therefore, $K_{iron} = 0$, as shown in Fig. 4(a). In this article, the equivalent virtual current sheet K_{iron} is introduced to represent the PMs, winding current, and iron saturation. To keep the airgap field unchanged and avoid calculating the permeability of the iron in the analytical model, H_{t_iron} is replaced by K_{iron} , as shown in Fig. 4(b). It is noted that the permeability of iron becomes infinite after the transformation as $H_{t_iron} = 0$. Hence, the modified boundary condition is shown as

$$\begin{cases} B_{r_air} = B_{r_iron} \\ H_{t_air} = K_{iron} \end{cases} \quad (8)$$

In order to solve governing Laplace equation for the airgap region using the conformal mapping model, surface current sheet K_{iron} in (8) can be regarded as uniformly distributed dot currents for simplicity, as shown in Fig. 4(b). Based on Ampere's law, the dot currents are calculated by [20], [21]

$$I_1 = I_2 = \dots = I_n = \frac{V_1 - V_2}{n} \quad (9)$$

where V_1 and V_2 are obtained from the mesh cell of Fig. 2. Accordingly, the equivalent dot currents along the rotor surface, which represent the PM and rotor saturation, can be equivalently calculated from the magnetic potential distribution of modular mesh cells on the rotor surface, as shown in Fig. 3(b).

Unlike the SPM motor, whose PM equivalent current is located along the PM edge in the airgap and should be transformed at every rotor position using the exact conformal mapping [30], the PM equivalent current of the IPM motor is placed on the rotor surface and stays unchanged at any rotor position. Therefore, the conformal mapping calculation is required only at the initial rotor position. Much calculation will be saved compared with the analytical calculation in the SPM motor.

In the proposed IHFM, five transformations are used to convert the slotted annular domain to the rectangular domain for the airgap region using the simplified one-slot model, as shown in Fig. 5. Take the position $r_s e^{j\alpha_s}$ in the complex plane of the original S domain as an example, it will be transformed to z_{full} in the Z_{full} domain using the logarithmic mapping, as shown in Fig. 5(a) and (b), where $z_{full} = \log(r_s) + j\alpha_s$. Then the position z_{full} is transformed to z_{slot} corresponding to Fig. 5(b)

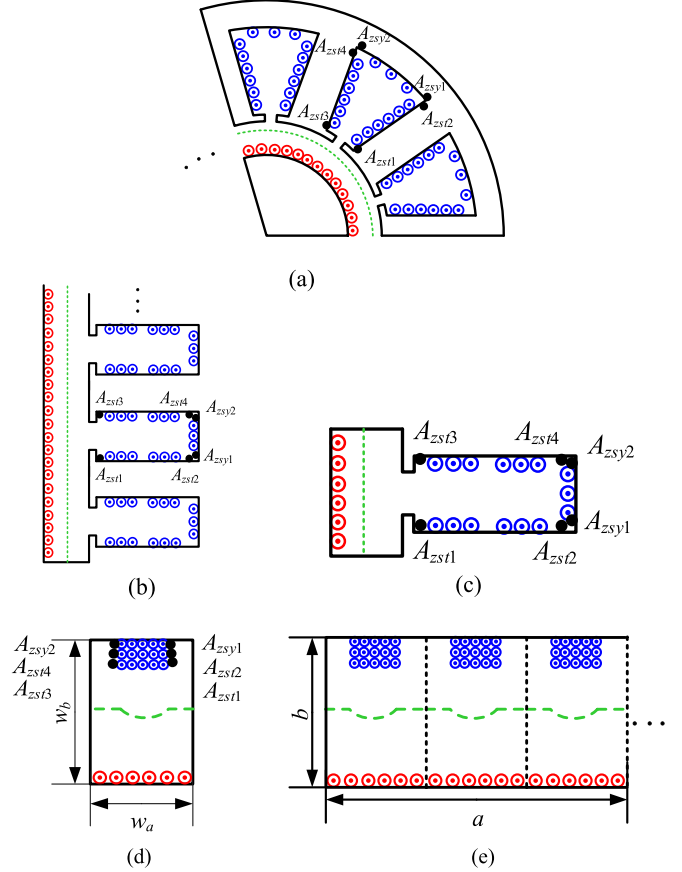


Fig. 5. Conformal mapping model based on the one-slot region. (a) S domain. (b) Z_{full} domain. (c) Z_{slot} domain. (d) W_{slot} domain. (e) W_{full} domain.

and (c) using the following equation:

$$\begin{aligned} z_{slot} &= \text{Re}(z_{full}) + i * (\text{Im}(z_{full}) \% (2\pi/Q_s)) \\ &= \log(r) + i * (a \% (2\pi/Q_s)). \end{aligned} \quad (10)$$

Next, the position z_{slot} in the polygon of Z_{slot} domain can be transformed into the position w_{slot} in the rectangle of W_{slot} domain using the inverse Schwarz–Christoffel (SC) mapping [31]

$$z_{slot} = A_0 \int \prod_{k=1}^{n-1} (w_{slot} - w_k)^{-\frac{\alpha_k}{\pi} - 1} dw + C_0. \quad (11)$$

Since it is difficult to directly solve the SC parameter in the mapping, the SC toolbox is employed to calculate the position w_{slot} in the W_{slot} domain, as shown in Fig. 5(c) and (d). It is noted that the SC mapping is the most time-consuming transformation as it requires the numerical calculation of nonlinear equation. However, by simplifying the multislots model to one-slot model, the calculation speed will be significantly improved. Then based on the periodicity of (10), the position w_{full} is obtained from w_{slot} using (12) for Fig. 5(d) and (e)

$$\begin{aligned} w_{full} &= [Q_s - 1 - \lfloor \text{Im}(z_{full}) / (2\pi/Q_s) \rfloor] * w_a \\ &\quad + \text{Re}(w_{slot}) + i * \text{Im}(w_{slot}). \end{aligned} \quad (12)$$

Based on these transformations, both current position and the path of the magnetic field can be determined in the S domain

and W_{full} domain. Hence, the vector potential $A_z(x, y)$ produced by the dot current $i_0(x_c, y_c)$ in the rectangular W_{full} domain can be calculated as [32]

$$A_z(x, y) = \frac{\mu_0 i_0}{2\pi} \left\{ \ln \left| e^{-c_\omega(ix+y+b/2)} - e^{-c_\omega(ix_c+y_c+b/2)} \right| - \sum_{k=1}^{+\infty} \frac{\cosh(c_\omega k(y-b)) + e^{kc_\omega(2y_c-b)} \cosh(kc_\omega y)}{k \sinh(kc_\omega b)} e^{-c_\omega k y_c} \cos[c_\omega k(x-x_c)] \right\} \quad (13)$$

where $c_w = 2\pi/a$, $a = Q_s * w_a$, $b = w_b$. w_a and w_b are the length and width of the rectangle in the W_{slot} domain. The flux densities in the x and y direction are calculated according to the vector potential in the W_{full} domain

$$B_{xw} = \frac{\partial A_z(x, y)}{\partial y}$$

$$B_{yw} = -\frac{\partial A_z(x, y)}{\partial x}. \quad (14)$$

Based on the conformal mapping theory, the magnetic field in the x and y directions of the S domain can be calculated from that in the W_{full} domain

$$B_s = B_{xs} + jB_{ys} = B_w \lambda_0 = (B_{xw} + jB_{yw}) \lambda_0 \quad (15)$$

where the complex permeance function λ_0 is expressed as

$$\lambda_0 = \frac{1}{\frac{\partial z}{\partial w}} \frac{1}{r_s e^{j\alpha_s}} \quad (16)$$

where $\frac{\partial z}{\partial w}$ is obtained from the SC transformation.

C. Improved Hybrid Field Model

The magnetic field of IPM motors cannot be determined directly because the analytical airgap field solution requires the equivalent dot current from the magnetic potential distribution in the proposed RNM, while the node flux source Φ in the RNM is calculated from the airgap field distribution. Hence, a solving loop is required to obtain the saturation level of stator and rotor iteratively. The solution of magnetic potential distribution \mathbf{V} in the nonlinear RN and MEC can be obtained according to Kirchhoff's law

$$f(\mathbf{V}) = \mathbf{A} \mathbf{A} \mathbf{A}^T \mathbf{V} - \mathbf{A} \mathbf{A} \mathbf{F}_{\text{sr}} - \Phi = 0 \quad (17)$$

where $\Phi = [\phi_{a1}, \dots, \phi_{sy1}, \dots, \phi_{st1}, \dots, \phi_{b1}, \dots]$. \mathbf{A} is the incidence matrix obtained from the RN and MECM. \mathbf{F}_{sr} consists of the magnetic voltage drop from PM and winding current. \mathbf{A} represents the iron reluctance matrix. As shown in Fig. 6, \mathbf{A} and \mathbf{V} will be iteratively solved. Hence, the magnetic field of IPM motors can be obtained at any rotor position by modifying the rotor position in (10)–(13).

The flux linkage of each phase is calculated from the airgap vector potential

$$\Psi_{ABC} = N_c \sum_{k=1}^{N_p} l_{\text{ef}} [A_{zk}(R_s, \alpha_1) - A_{zk}(R_s, \alpha_1 + 2\pi\tau/Q_s)] \quad (18)$$

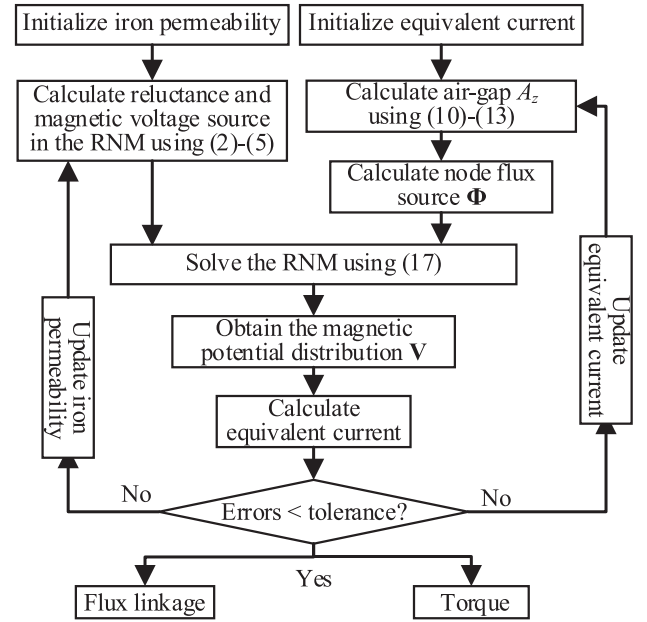


Fig. 6. Flowchart of solving process for any rotor position.

where R_s is the stator outer radius. τ is the slot pitch. N_p is the pair of the slot for each phase. α_1 and N_c are the initial angle of the coil and the number of coil belonging to each phase, respectively. Hence, the induced voltage of the IPM motor is expressed as

$$U_{ABC} = \frac{d\Psi_{ABC}}{dt}. \quad (19)$$

The electromagnetic torque is calculated according to the Maxwell tensor theory using the radial and tangential flux density in the air-gap

$$T_e = r l_{\text{ef}} \int_0^{2\pi} B_{r_air}(r, \alpha) B_{t_air}(r, \alpha) d\alpha \quad (20)$$

where α and r are the angle and radius of the circular integral path along the middle of the airgap region.

III. FE ANALYSIS AND EXPERIMENT

In this article, an 8-pole/36-slot V-type IPM motor and a 4-pole/24-slot flat-type IPM motor are designed and analyzed to validate the proposed model, as shown in Fig. 7. The IHFM predictions are compared with the FEM results and the experiment is carried out to show the calculation accuracy. The two prototype motors are shown in Figs. 7–9 and their main parameters are displayed in Table I. The nonlinear BH curves of the iron material are shown in Fig. 10. It is noted that the average flux density in the rotor bridge of both IPM motors is larger than 2.2 T at the rated load, which can be regarded as highly saturated, as shown in Fig. 7.

The interaction between slots is negligible due to the symmetrical structure of the stator and, therefore, the one-slot conformal mapping model has the same results as those from the exact conformal mapping, which transformed the whole

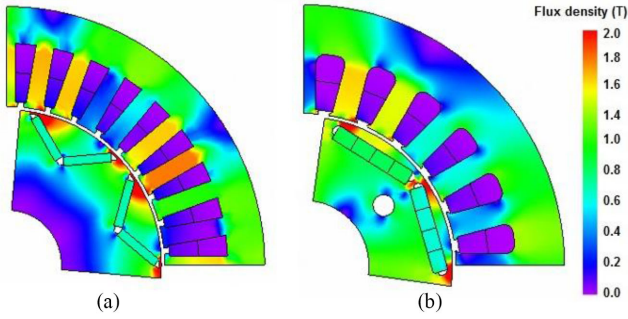


Fig. 7. Field distribution of IPM motors at the rated load. (a) V-type rotor. (b) Flat-type rotor.

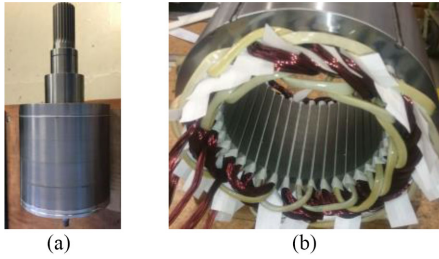


Fig. 8. Prototype 8-pole/36-slot V-type IPM motors. (a) V-type rotor. (b) Stator.

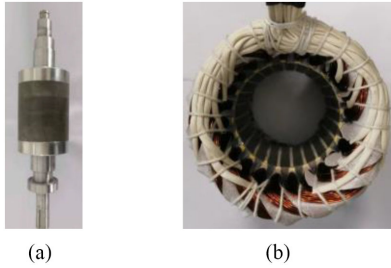


Fig. 9. Prototype 4-pole/24-slot flat-type IPM motors. (a) Flat-type rotor. (b) Stator.

TABLE I
MAIN PARAMETERS OF IPM MOTORS

Parameter	V-type IPM machine	flat-type IPM machine
Stator outer diameter	120mm	245mm
Magnet material	N35UH	N38H
Iron material	20JNEH1200	M235-35A
Rated speed	15000rpm	2800rpm

airgap region in the SC mapping. Besides, the accuracy of the one-slot conformal mapping model is compared with the FEM calculations neglecting the saturation effect. As shown in Fig. 1, seven dot currents locating in “A–G” are chosen to calculate the magnetic field in the middle of airgap using the one-slot conformal mappings and FEM, respectively. The average error for the radial and tangential airgap field of V-type IPM motor is less than 0.2% and 0.3%, as given in Table II. As for the flat-type IPM motor, they are less than 0.2% and 0.5% according to Table III. It is noted that the variation of slot opening has

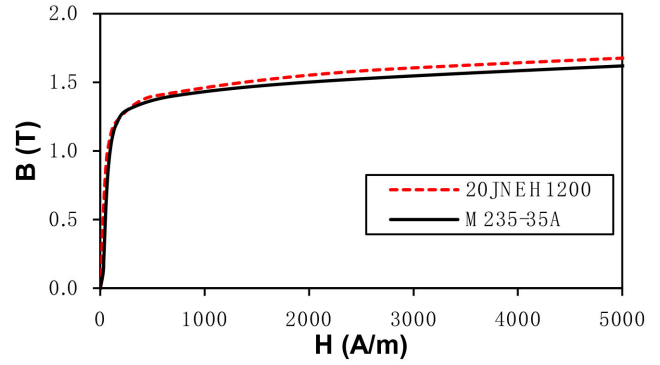


Fig. 10. BH curves of magnetic material for IPM motors.

TABLE II
AVERAGE ERROR OF MAGNETIC FIELD USING ONE-SLOT CONFORMAL MAPPING FOR V-TYPE IPM MOTOR (UNIT: %)

Slot opening	Flux density	A*	B*	D*	F*	G*
0.5mm	Radial	0.15	0.15	0.16	0.14	0.15
	Tangential	0.17	0.13	0.15	0.11	0.11
1mm	Radial	0.14	0.14	0.14	0.13	0.14
	Tangential	0.15	0.17	0.15	0.12	0.15
2mm	Radial	0.18	0.18	0.20	0.13	0.19
	Tangential	0.21	0.21	0.22	0.15	0.15
3mm	Radial	0.14	0.14	0.15	0.12	0.15
	Tangential	0.22	0.22	0.26	0.15	0.19
4mm	Radial	0.11	0.11	0.13	0.08	0.12
	Tangential	0.26	0.26	0.29	0.17	0.17

*The position “A–G” are defined in Fig. 1.

TABLE III
AVERAGE ERROR OF MAGNETIC FIELD USING ONE-SLOT CONFORMAL MAPPING FOR FLAT-TYPE IPM MOTOR (UNIT: %)

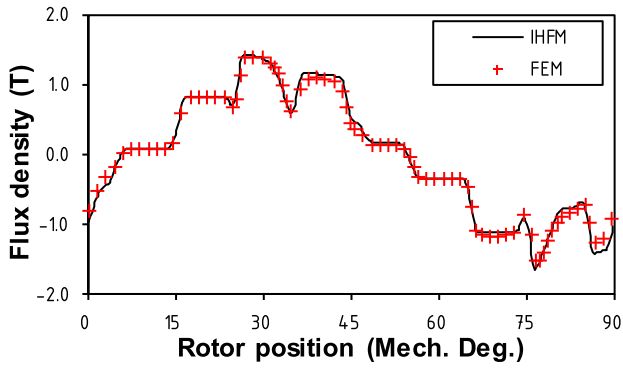
Slot opening	Flux density	A	B	D	F	G
0.5mm	Radial	0.10	0.10	0.10	0.11	0.10
	Tangential	0.09	0.09	0.09	0.11	0.11
1mm	Radial	0.09	0.09	0.10	0.11	0.09
	Tangential	0.13	0.13	0.13	0.13	0.13
2mm	Radial	0.04	0.04	0.05	0.08	0.05
	Tangential	0.38	0.38	0.28	0.22	0.23
3mm	Radial	0.07	0.07	0.08	0.09	0.09
	Tangential	0.49	0.49	0.49	0.28	0.25

a negligible influence on the accuracy of one-slot conformal mapping.

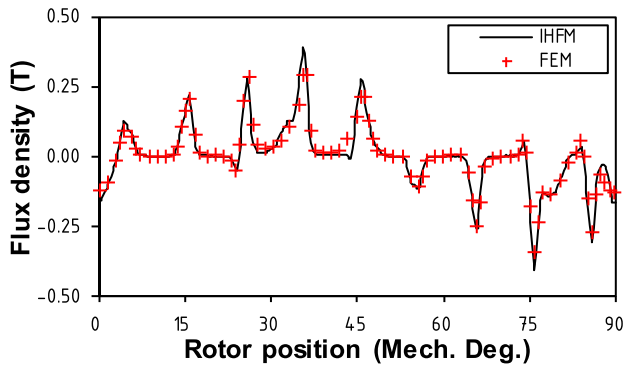
The saturation effect is investigated using IHFM. For the V-type IPM motor, there are 160 and 400 modular mesh cells for the pole-shoe region and rotor surface, respectively. As for the flat-type IPM motor, they become 80 and 168, respectively.

The V-type IPM motor is operated with the current angle of 20° and the input current is 200 A. The flat-type IPM motor runs using the maximum torque per ampere (MTPA) control, whose current angle is 16° and the input current is 47 A. Under this load condition, the flux densities of both IPM motors are calculated using IHFM in Figs. 11 and 12, and their results show great agreement with FEM calculations.

The flux linkage and induced voltage of both IPM motors using IHFM are consistent with FEM results under the on-load condition, as shown in Figs. 13–16. The average errors of flux

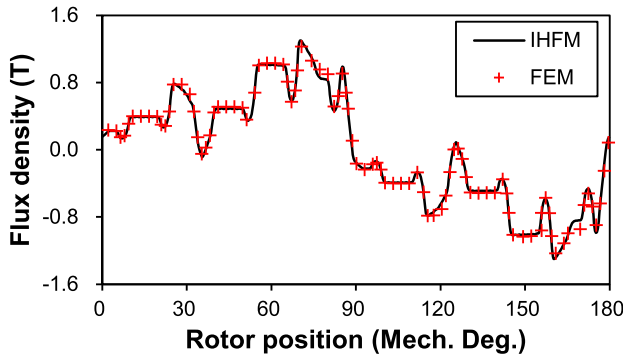


(a)

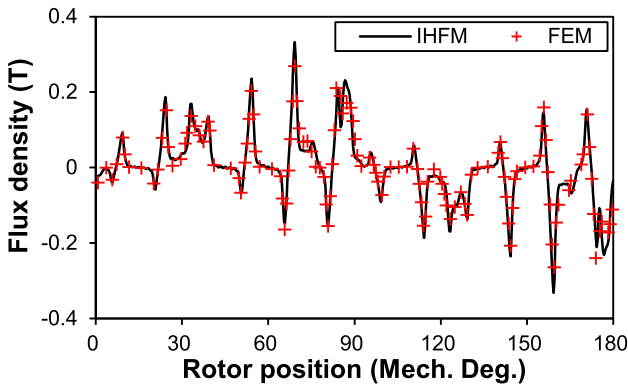


(b)

Fig. 11. Airgap filed distribution of V-type IPM motor at 164 N-m. (a) Radial flux density. (b) Tangential flux density.



(a)



(b)

Fig. 12. Airgap filed distribution of flat-type IPM motor at 8.7 N-m. (a) Radial flux density. (b) Tangential flux density.

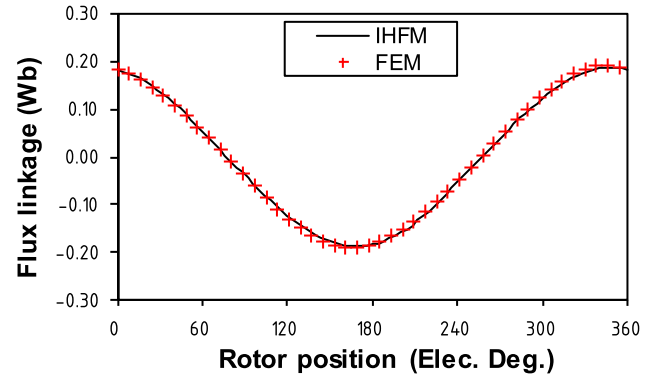


Fig. 13. Flux linkage waveform of the V-type IPM motor at 164 N-m with the current angle of 20°.

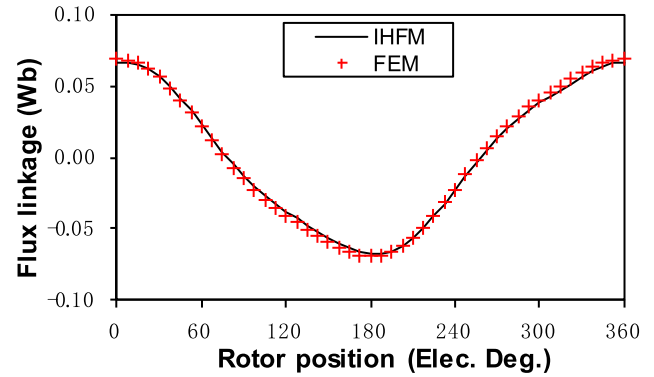


Fig. 14. Flux linkage waveform of the flat-type IPM motor at 8.7 N-m using the MTPA control.

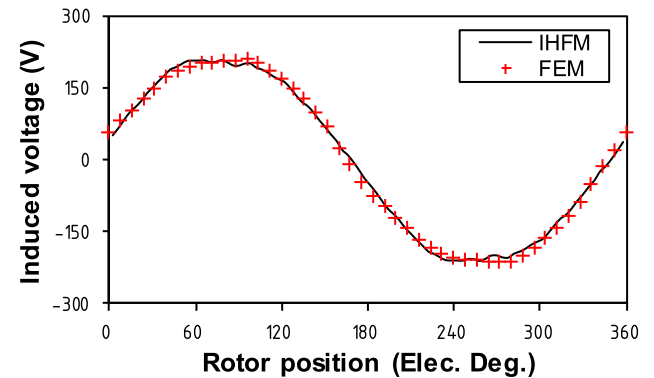


Fig. 15. Induced voltage waveform of the V-type IPM motor at 164 N-m with the current angle of 20°.

linkage using IHFM for the V-type and flat-type IPM motors are 1.9% and 2.5%, respectively. As for the induced voltage, the average errors for the V-type and flat-type IPM motors are 3.3% and 2.2%, respectively. Hence, it is demonstrated that the IHFM can accurately predict the induced voltage of IPM motors considering the armature reaction.

In Fig. 17, the torque waveforms using IHFM are similar to the FEM calculations, the average torque error for the V-type IPM motors is less than 0.5%. In Fig. 18, IHFM predicts a higher torque value than the FEM prediction; however, it should be noted that the average torque error of the IHFM prediction is

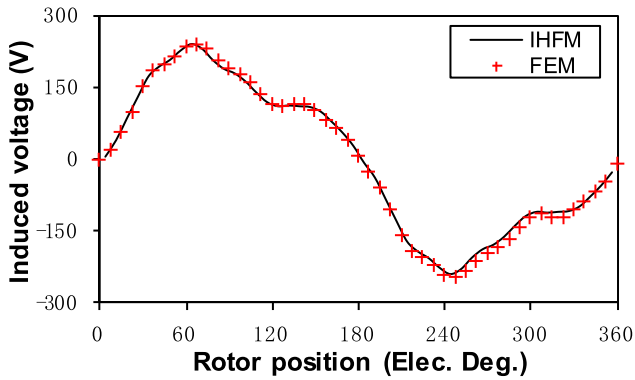


Fig. 16. Induced voltage waveform of the flat-type IPM motor at 8.7 N-m using the MTPA control.

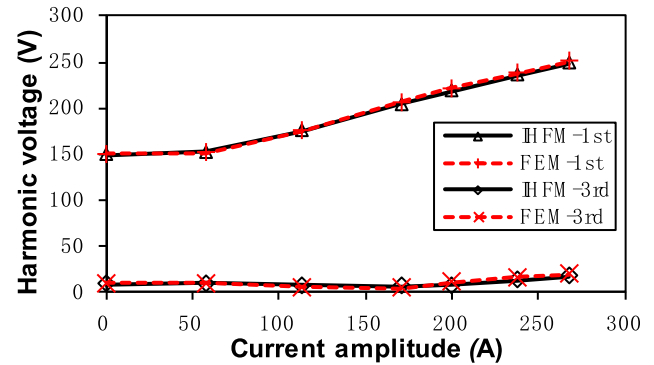


Fig. 19. Variation of induced harmonic voltage with the phase current amplitude using the current angle of 20° for the V-type IPM motor.

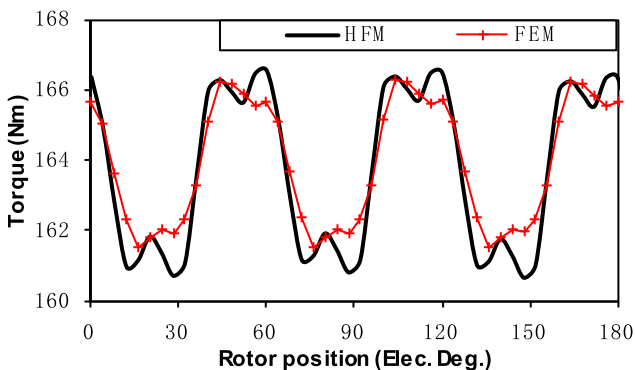


Fig. 17. Torque waveform of the V-type IPM motor at 164 N-m with the current angle of 20° .

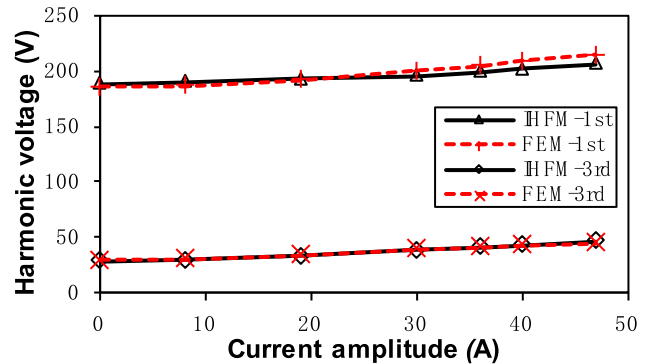


Fig. 20. Variation of induced harmonic voltage with the phase current amplitude using the MTPA control for the flat-type IPM motor.

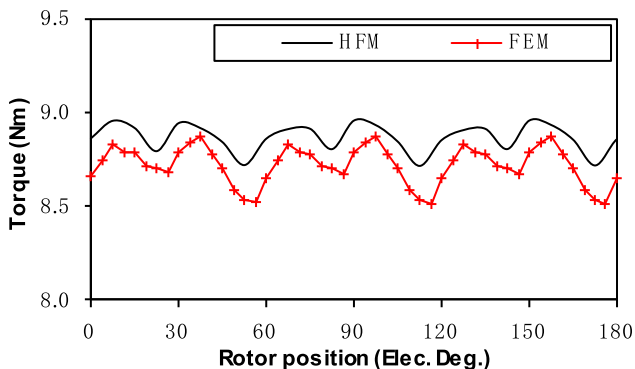


Fig. 18. Torque waveform of the flat-type IPM motor at 8.7 N-m using the MTPA control.

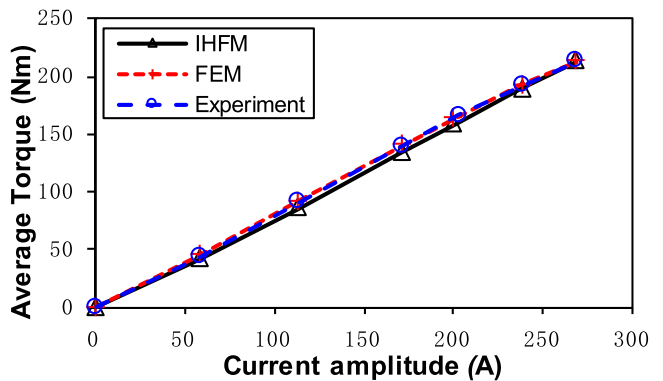


Fig. 21. Variation of average torque with the phase current amplitude using the current angle of 20° for the V-type IPM motor.

less than 1.7%, which is rather small and acceptable. The differences in electromagnetic performance calculation using IHFM and FEM come from the simplification of iron modeling using MECM and RNM to achieve a high computational efficiency.

In order to investigate the influence of the armature field on the induced voltage and electromagnetic torque, IHFM is employed to calculate the magnetic field of IPM motors under different load condition. The flat-type IPM motor is operated using the MTPA control strategy, while the V-type IPM motor runs with

the current angle of 20° . The major and third harmonic voltages are calculated using IHFM for both IPM motors, as shown in Figs. 19 and 20. IHFM predictions agree well with the FEM results, which mean the proposed model can accurately describe the induced voltage. The average torque under a different load condition is calculated for both IPM motors in Figs. 21 and 22. Both FEM calculations and experimental results are close to IHFM predictions regardless of the amplitude of the winding current. The torque error of IHFM is less than 5% for both IPM motors according to the experiment results.

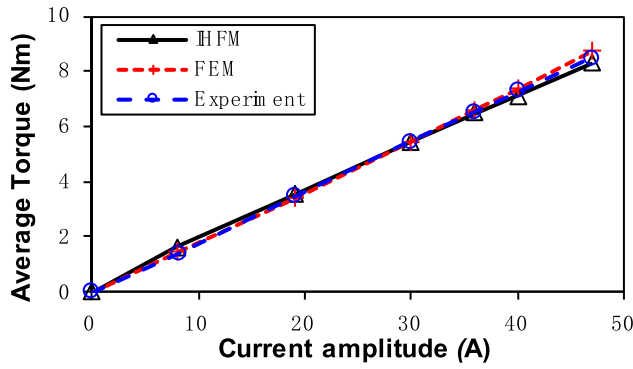


Fig. 22. Variation of average torque with the phase current amplitude using the MTPA control for the flat-type IPM motor.

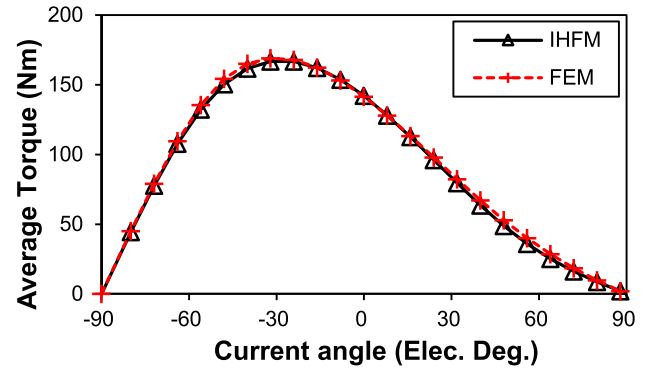


Fig. 25. Variation of average torque with the current angle for the V-type IPM motor.

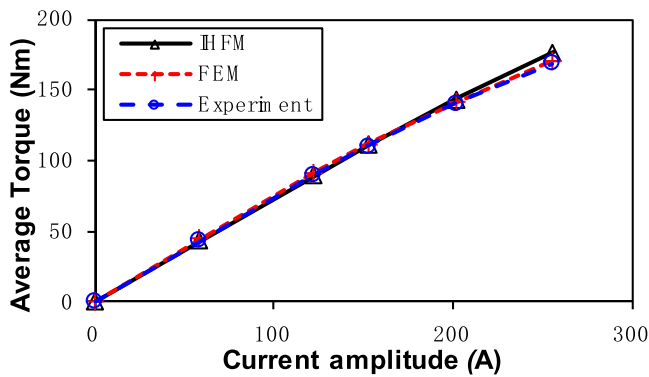


Fig. 23. Variation of average torque with the phase current amplitude using $i_d = 0$ control for the V-type IPM motor.

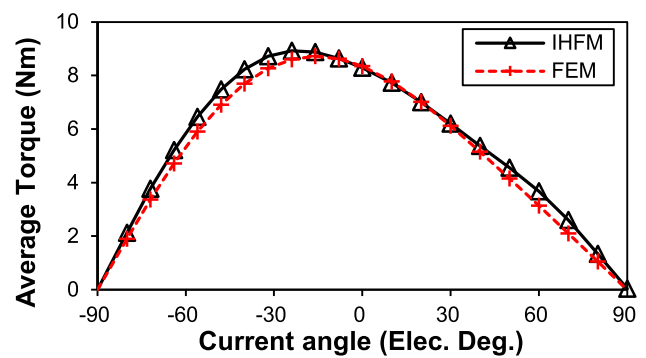


Fig. 26. Variation of average torque with the current angle for the flat-type IPM motor.

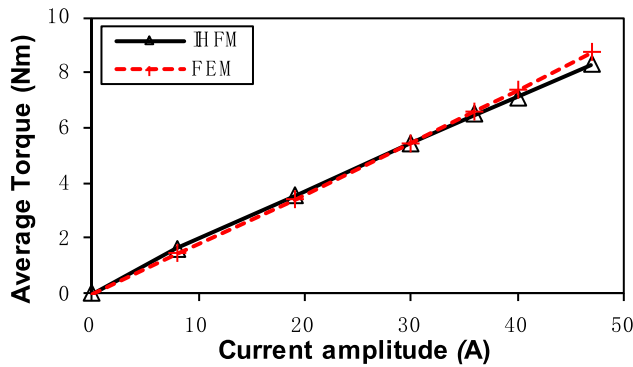


Fig. 24. Variation of average torque with the phase current amplitude using $i_d = 0$ control for the flat-type IPM motor.

The IPM motors are operated using $i_d = 0$ control to verify the proposed model under a different control strategy. The experiment is carried out for the V-type IPM motor and its result compared with the IHFM and FEM calculations in Fig. 23. The torque error is less than 5%, which shows the high accuracy of IHFM under $i_d = 0$ operation. Besides, Fig. 24 shows that the IHFM can accurately predict the torque for the flat-type IPM motor using $i_d = 0$ control and the torque error is less than 5%.

Besides, the IHFM shows great accuracy in calculating the torque at a different current angle for both IPM motors, as shown

TABLE IV
SIMULATION SETTING FOR IPM MOTORS

IPM motor	Model	Air-gap division	Calculation steps	Total Node	Air-gap Node
V-type	IHFM	180	90	269	0
	FEM			2916	720
flat-type	IHFM	288	96	320	0
	FEM			5410	1151

in Figs. 25 and 26. The average error of the IHFM prediction for the V-type IPM motor is less than 1.9%, while it is less than 4.5% for the flat-type IPM motor. Larger errors are observed for the flat-type IPM motor due to the simplified modeling of the iron region between PMs using MECM, which can be much saturated when the current angle is large and, therefore, significantly influences the torque. As for the V-type IPM motor, the iron region between PMs is large enough to avoid saturation regardless of the current angle. Hence, it can be concluded that the IHFM is suitable to calculate the torque-angle performances for IPM motors with a large iron region between PMs or to calculate the torque characteristic of IPM motors using the MTPA control. The work of analytical modeling for IPM motors with a small iron region between PMs using the flux-weakening control will be presented in the future.

The time efficiency is compared in Tables IV–VI. The same parameters are set to utilize IHFM in the Matlab platform and

TABLE V
CALCULATION TIME OF IHFM AND FEM FOR V-TYPE IPM MOTOR

Current (A)	0	57.7	113	171	200	238	268
HFM (s)	71	76	81	94	99	117	126
FEM (s)	1106	1174	1182	1223	1243	1278	1294

TABLE VI
CALCULATION TIME OF IHFM AND FEM FOR FLAT-TYPE IPM MOTOR

Current (A)	0	8	19	30	36	40	47
HFM (s)	94	102	103	103	112	115	117
FEM (s)	898	903	903	906	917	926	940

FEM in the commercial software for motor design (JMAG), respectively, as given in Table IV. In Table V, the IHFM consumes less than one-tenth of the calculation time using FEM for the V-type IPM motor. Besides, the calculation time using IHFM is less than one-eighth of that using FEM for the flat-type IPM motor, as given in Table VI. Hence, IHFM has a great advantage in the calculation speed compared with FEM.

IV. CONCLUSION

This article developed an IHFM for predicting the on-load electromagnetic performance of IPM motors. Both MECM and RNM were used to represent the iron region in terms of the calculation accuracy and calculation time. The equivalent virtual currents calculated from the magnetic potential drop in the iron region were introduced to obtain the analytical airgap solution. Meanwhile, the novel mesh cell with the airgap flux source from the analytical model will form the RN and MEC of stator and rotor efficiently. The analytical model based on the one-slot conformal mapping was proposed to improve the efficiency of calculation. Owing to the stationary airgap region in IPM motors, the conformal mapping was required only once while considering the position change of equivalent virtual current and the path in the transformation of the airgap region. Both FEM calculation and experimental results of the flat-type and V-type IPM motors demonstrate the high accuracy of IHFM with a reduced computational burden to the greatest extent.

REFERENCES

- [1] B. Guo, Y. Huang, F. Peng, and J. Dong, "A new hybrid method for magnetic field calculation in IPMSM accounting for any rotor configuration," *IEEE Trans. Ind. Electron.*, vol. 66, no. 7, pp. 5015–5024, Jul. 2019.
- [2] L. Zhu, S. Z. Jiang, Z. Q. Zhu, and C. C. Chan, "Analytical modeling of open-circuit air-gap field distributions in multisegment and multilayer interior permanent-magnet machines," *IEEE Trans. Magn.*, vol. 45, no. 8, pp. 3121–3130, Aug. 2009.
- [3] X. Huang, M. Zhu, W. Chen, J. Zhang, and Y. Fang, "Dynamic reluctance mesh modeling and losses evaluation of permanent magnet traction motor," *IEEE Trans. Magn.*, vol. 53, no. 6, Jun. 2017, Art. no. 8102804.
- [4] K. Nakamura, K. Saito, and O. Ichinokura, "Dynamic analysis of interior permanent magnet motor based on a magnetic circuit model," *IEEE Trans. Magn.*, vol. 39, no. 5, pp. 3250–3252, Sep. 2003.
- [5] H.-K. Yeo, D.-K. Lim, and H.-K. Jung, "Magnetic equivalent circuit model considering the overhang structure of an interior permanent-magnet machine," *IEEE Trans. Magn.*, vol. 55, no. 6, Jun. 2019, Art. no. 8201404.
- [6] G. Liu, Y. Wang, Q. Chen, G. Xu, and D. Cao, "Design and analysis of a new equivalent magnetic network model for IPM machines," *IEEE Trans. Magn.*, vol. 56, no. 6, Jun. 2020, Art. no. 8101112.
- [7] S. Jiang, G. Liu, W. Zhao, L. Xu, and Q. Chen, "Modeling and analysis of spoke-type permanent magnet vernier machine based on equivalent magnetic network method," *Chin. J. Elect. Eng.*, vol. 4, no. 2, pp. 96–103, 2018.
- [8] G. Liu, S. Jiang, W. Zhao, and Q. Chen, "Modular reluctance network simulation of a linear permanent-magnet Vernier machine using new mesh generation methods," *IEEE Trans. Ind. Electron.*, vol. 64, no. 7, pp. 5323–5332, Jul. 2017.
- [9] T. A. Lipo, *Analysis of Synchronous Machines*. Boca Raton, FL, USA: CRC Press, 2017.
- [10] K.-T. Kim, J.-K. Park, J. Hur, and B.-W. Kim, "Comparison of the fault characteristics of IPM-type and SPM-type BLDC motors under inter-turn fault conditions using winding function theory," *IEEE Trans. Ind. Appl.*, vol. 50, no. 2, pp. 986–994, Mar./Apr. 2014.
- [11] H. Chen, D. Li, R. Qu, Z. Zhu, and J. Li, "An improved analytical model for inductance calculation of interior permanent magnet machines," *IEEE Trans. Magn.*, vol. 50, no. 6, Jun. 2014, Art. no. 7027108.
- [12] Q. Li, T. Fan, and X. Wen, "Armature-reaction magnetic field analysis for interior permanent magnet motor based on winding function theory," *IEEE Trans. Magn.*, vol. 49, no. 3, pp. 1193–1201, Mar. 2013.
- [13] M. Farshadnia, M. A. M. Cheema, R. Dutta, and J. E. Fletcher, "Analytical modeling of armature reaction air-gap flux density considering the non-homogeneously saturated rotor in a fractional-slot concentrated-wound IPM machine," *IEEE Trans. Magn.*, vol. 53, no. 2, Feb. 2017, Art. no. 8200412.
- [14] A. Balamurali, C. Lai, A. Mollaeian, V. Loukanov, and N. C. Kar, "Analytical investigation into magnet eddy current losses in interior permanent magnet motor using modified winding function theory accounting for pulsewidth modulation harmonics," *IEEE Trans. Magn.*, vol. 52, no. 7, Jul. 2016, Art. no. 8106805.
- [15] H. Gurleyen and E. Mese, "A nonlinear q -axis inductance modeling of a 12-slot 10-pole IPM using approximate analytical methods," *IEEE Trans. Energy Convers.*, vol. 35, no. 2, pp. 621–630, Jun. 2020.
- [16] N. Elloumi, M. Bortolozzi, A. Masmoudi, M. Mezzarobba, M. Olivo, and A. Tassarolo, "Numerical and analytical approaches to the modeling of a spoke type IPM machine with enhanced flux weakening capability," *IEEE Trans. Ind. Appl.*, vol. 55, no. 5, pp. 4702–4714, Sep./Oct. 2019.
- [17] A. Tassarolo, "Accurate computation of multiphase synchronous machine inductances based on winding function theory," *IEEE Trans. Energy Convers.*, vol. 27, no. 4, pp. 895–904, Dec. 2012.
- [18] K. Ramakrishnan, D. Zarko, A. Hanic, and G. Mastinu, "Improved method for field analysis of surface permanent magnet machines using Schwarz–Christoffel transformation," *IET Electr. Power Appl.*, vol. 11, no. 6, pp. 1067–1075, Jul. 2017.
- [19] L. J. Wu, Z. Li, X. Huang, Y. Zhong, Y. Fang, and Z. Q. Zhu, "A hybrid field model for open-circuit field prediction in surface-mounted PM machines considering saturation," *IEEE Trans. Magn.*, vol. 54, no. 6, Jun. 2018, Art. no. 8103812.
- [20] L. J. Wu, Z. Li, D. Wang, H. Yin, X. Huang, and Z. Q. Zhu, "On-load field prediction of surface-mounted pm machines considering nonlinearity based on hybrid field model," *IEEE Trans. Magn.*, vol. 55, no. 3, Mar. 2019, Art. no. 8100911.
- [21] L. Wu, H. Yin, D. Wang, and Y. Fang, "A nonlinear subdomain and magnetic circuit hybrid model for open-circuit field prediction in surface-mounted PM machines," *IEEE Trans. Energy Convers.*, vol. 34, no. 3, pp. 1485–1495, Sep. 2019.
- [22] L. Wu, H. Yin, D. Wang, and Y. Fang, "On-load field prediction in SPM machines by a subdomain and magnetic circuit hybrid model," *IEEE Trans. Ind. Electron.*, vol. 67, no. 9, pp. 7190–7201, Sep. 2020.
- [23] P. Liang, F. Chai, Y. Li, and Y. Pei, "Analytical prediction of magnetic field distribution in spoke-type permanent-magnet synchronous machines accounting for bridge saturation and magnet shape," *IEEE Trans. Ind. Electron.*, vol. 64, no. 5, pp. 3479–3488, May 2017.
- [24] P. Liang, F. Chai, Y. Yu, and L. Chen, "Analytical model of a spoke-type permanent magnet synchronous in-wheel motor with trapezoid magnet accounting for tooth saturation," *IEEE Trans. Ind. Electron.*, vol. 66, no. 2, pp. 1162–1171, Feb. 2019.
- [25] M. S. Mirazimi and A. Kiyomarsi, "Magnetic field analysis of multi-flux-barrier interior permanent-magnet motors through conformal mapping," *IEEE Trans. Magn.*, vol. 53, no. 12, Dec. 2017, Art. no. 7002512.
- [26] D. Lim *et al.*, "Analysis and design of a multi-layered and multi-segmented interior permanent magnet motor by using an analytic method," *IEEE Trans. Magn.*, vol. 50, no. 6, Jun. 2014, Art. no. 8201308.

- [27] Z. Li, X. Huang, L. Wu, T. Long, B. Shi, and H. Zhang, "Open-circuit field prediction of interior permanent-magnet motor using hybrid field model accounting for saturation," *IEEE Trans. Magn.*, vol. 55, no. 7, Jul. 2019, Art. no. 8104707.
- [28] P. Liang, F. Chai, Y. Bi, Y. Pei, and S. Cheng, "Analytical model and design of spoke-type permanent-magnet machines accounting for saturation and nonlinearity of magnetic bridges," *J. Magn. Magn. Mater.*, vol. 417, pp. 389–396, 2016.
- [29] Z. Zhang, C. Xia, Y. Yan, Q. Geng, and T. Shi, "A hybrid analytical model for open-circuit field calculation of multilayer interior permanent magnet machines," *J. Magn. Magn. Mater.*, vol. 435, pp. 136–145, 2017.
- [30] A. Hanic, D. Zarko, D. Kuhinek, and Z. Hanic, "On-load analysis of saturated surface permanent magnet machines using conformal mapping and magnetic equivalent circuits," *IEEE Trans. Energy Convers.*, vol. 33, no. 3, pp. 915–924, Sep. 2018.
- [31] T. C. O'Connell and P. T. Krein, "A Schwarz–Christoffel-based analytical method for electric machine field analysis," *IEEE Trans. Energy Convers.*, vol. 24, no. 3, pp. 565–577, Sep. 2009.
- [32] B. Hague, *The Principles of Electromagnetism Applied to Electrical Machines*. New York, NY, USA: Dover, 1962.



Zhaokai Li was born in Lishui, China, in 1993. He received the B.S. and Ph.D. degrees in electrical engineering from Zhejiang University, Hangzhou, China, in 2015 and 2020, respectively.

He is currently a Postdoctoral Researcher with the College of Electrical Engineering, Zhejiang University, Hangzhou. His major research interests include the analytical modeling of PMSM and iron loss analysis.



Xiaoyan Huang (Member, IEEE) received the B.E. degree in control measurement techniques and instrumentation from Zhejiang University, Hangzhou, China, in 2003, and the Ph.D. degree in electrical machines and drives from the University of Nottingham, Nottingham, U.K., in 2008.

From 2008 to 2009, she was a Research Fellow with the University of Nottingham. She is currently a Professor with the College of Electrical Engineering, Zhejiang University, Hangzhou,

China, where she is working on electrical machines and drives. Her research interests include PM machines and drives for aerospace and traction applications, and generator system for urban networks.



Lijian Wu (Senior Member, IEEE) received the B.Eng. and M.Sc. degrees from the Hefei University of Technology, Hefei, China, in 2001 and 2004, respectively, and the Ph.D. degree from The University of Sheffield, Sheffield, U.K., in 2011, all in electrical engineering.

Since 2016, he has been with Zhejiang University, Hangzhou, China, where he is currently a Professor of electrical machines and control systems. His current research interests include the design and control of PM machines.



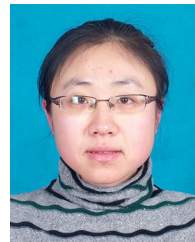
He Zhang (Senior Member, IEEE) received the B.Eng. degree in control science and engineering from Zhejiang University, Hangzhou, China, in 2002, and the M.Sc. and Ph.D. degrees in electrical machines from the University of Nottingham, Nottingham, U.K., in 2004 and 2009, respectively.

He is currently the Director with the Nottingham Electrification Centre, Power Electronics, Machines, and Control Research Group, University of Nottingham, Nottingham. His research interests include high-performance electric machines and drives for transport electrification.



Tingna Shi (Member, IEEE) was born in Yuyao, China, in 1969. She received the B.S. and M.S. degrees from Zhejiang University, Hangzhou, China, in 1991 and 1996, respectively, and the Ph.D. degree from Tianjin University, Tianjin, China, in 2009, all in electrical engineering.

She is currently a Professor with the College of Electrical Engineering, Zhejiang University, Hangzhou, China. Her current research interests include electrical machines and their control systems, power electronics, and electric drives.



Yan Yan was born in Tianjin, China, in 1981. She received the B.S. and M.S. degrees from the Tianjin University of Science and Technology, Tianjin, China, in 2004 and 2007, respectively, and the Ph.D. degree from Tianjin University, Tianjin, China, in 2010, all in electrical engineering.

She is currently an Associate Professor with the College of Electrical Engineering, Zhejiang University, Hangzhou, China. Her current research interests include electrical machines and

their control systems, power electronics, and electric drives.



Bowen Shi was born in Hangzhou, China, in 1990. He received the B.S. and Ph.D. degrees in electrical engineering from the University of Nottingham, Nottingham, U.K., in 2013 and 2018, respectively.

He is currently a Senior Engineer with Nottingham Electrification Center, University of Nottingham, Nottingham, and a Postdoctoral Researcher with the College of Electrical Engineering, Zhejiang University, Hangzhou. His main research interest is the PMSM design for traction applications.



Geng Yang (Member, IEEE) received the B.Sc. and M.Sc. degrees in control measurement techniques and instrumentation from the College of Biomedical Engineering and Instrument Science, Zhejiang University (ZJU), Hangzhou, China, in 2003 and 2006, respectively, and the Ph.D. degree in electronic and computer systems from the KTH Royal Institute of Technology, Stockholm, Sweden, in 2013.

He is currently a Research Professor with the School of Mechanical Engineering, ZJU, Hangzhou, China. He developed low power, low noise bioelectric SoC sensors for *m*-health. His research interests include flexible and stretchable electronics, mixed-mode IC design, low-power biomedical microsystem, wearable biodevices, human–computer interface, human–robot interaction, intelligent sensors, and the Internet of Things for healthcare.